Optical Engineering 48(10), 105602 (October 2009)

Spatial heterodyne spectroscopy for long-wave infrared: first measurements of broadband spectra

Christoph R. Englert
Naval Research Laboratory
Space Science Division
4555 Overlook Avenue South West
Washington, DC 20375
E-mail: christoph.englert@nrl.navy.mil

David D. Babcock
Artep Inc.
2922 Excelsior Springs Court
Ellicott City, Maryland 21042

John M. Harlander, MEMBER SPIE
St. Cloud State University
Department of Physics
Astronomy and Engineering
St. Cloud, Minnesota 56301

Abstract. We describe the design and implementation of a long-wave infrared (LWIR) spectrometer based on the spatial heterodyne spectroscopy (SHS) technique, and present the first measurements of broadband LWIR spectra taken with an SHS instrument. This work represents the first successful application of SHS to the field of LWIR spectroscopy, which is currently dominated by Fourier transform spectrometers, grating spectrometers, and Fabry-Perot interferometers. A unique combination of properties makes SHS a valuable addition to the existing types of LWIR spectrometers. Most notable are the interferometric throughput (no slit), lack of moving parts, and that the measured spectra are not contaminated by a changing scene, which makes SHS particularly suitable for applications in rugged environments and on moving platforms. The instrument discussed here is called the Spatial Heterodyne Imager for Chemicals and Atmospheric Detection (SHIMCAD), and is designed to cover the wavelength range between about 8.4 μm (1190 cm^{-1}) and 11.2 μm (890 cm^{-1}) with a spectral resolution of about 4 cm^{-1}. First, laboratory SHS transmission spectra of methanol and polyimide (Kapton®) are presented. The instrument is built to be mobile, so that ultimately field measurements can be conducted. [DOI: 10.1117/1.3250194]

Subject terms: spectroscopy; spectrometer; infrared; long-wave infrared; spatial heterodyne spectroscopy; remote sensing; atmosphere.

Paper 090510R received Jul. 9, 2009; revised manuscript received Aug. 31, 2009; accepted for publication Aug. 31, 2009; published online Oct. 30, 2009.

1 Introduction

High-resolution, passive, long-wave infrared (LWIR) spectroscopy has numerous civilian and military applications. Many of these applications take advantage of unique spectral emission or absorption signatures of solids, liquids, and gasses in the thermal infrared. The spectral region between about 7 and 20 μm is known as the "fingerprint region," since many of these characteristic spectral features, like ro-vibrational molecular lines, are contained in this wavelength interval.

Generally, different measurement techniques are employed in the LWIR depending on the specific requirements of the application. The width of the spectral coverage (passband), spectral resolution, sensitivity, and imaging needs are a few examples of requirements that need to be considered when choosing a measurement technique or instrument for a specific application. Common measurement techniques are grating spectrometers,[1] imaging and nonimaging Fourier transform spectrometers (FTS),[2–6] Fabry-Perot interferometers,[7] and prism spectrographs.[8]

Here we describe the Spatial Heterodyne Imager for Chemicals and Atmospheric Detection (SHIMCAD), a spatial heterodyne spectroscopy (SHS) instrument for the LWIR. The fundamental principles underlying SHS and its basic properties have been presented previously by Harlander, Reynolds, and Roesler.[9] SHS was first utilized for high spectral resolution measurements of diffuse sources in the ultraviolet.[9,10] For these applications, when compared to other conventional spectroscopic techniques, the main advantages of SHS are the high interferometric throughput, high spectral resolution, the compact, rugged package, and the relaxed alignment and fabrication tolerances. Other recent SHS instrument developments for the UV and visible include spectrometers for satellite remote sensing of the Earth's atmosphere,[11] astrophysics,[12] and laboratory spectroscopy.[13] The main motivation to demonstrate SHS in the LWIR is that SHS allows the same high throughput as a field-widened FTS in a rugged package without moving parts, while being insensitive to any scene changes during the single exposure measurement. Moreover, it allows 1-D imaging, so when used in a pushbroom-type observation, 2-D imaging can be achieved. The insensitivity to scene changes is an important advantage over scanning techniques like FTS, which require the scene to be constant over multiple exposures. On moving platforms, like airplanes or ground vehicles, this limitation results in the requirement for very short exposures and/or motion compensation with stabilization platforms, and vibration damping for the reduction of jitter. For example, in a nadir-looking airplane geometry, these precautions can ensure that the instrument views the same location during the FTS scan, but scene changes due to the view angle variation may still

0091-3286/2009/$25.00

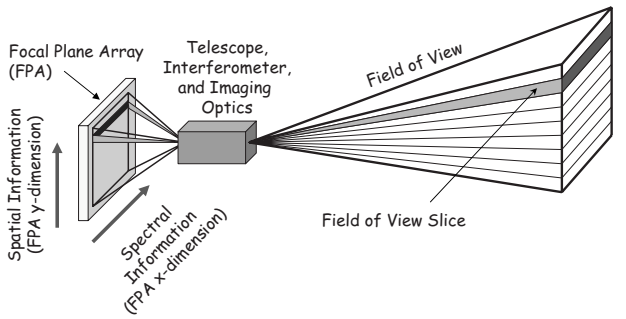

Fig. 1 Sketch of how SHIMCAD records spectral and spatial information from an observed scene. The vertical dimension is imaged on the detector, preserving the spatial information, while the horizontal dimension of the scene is out of focus at the detector, so that spatial scene variations do not contaminate the spectral information.

be present and may cause a contamination of the retrieved spectrum. The fact that SHS does not need any moving parts also avoids many difficulties in field hardening the instrument; that is to ensure that a rough mechanical environment does not decrease the quality of the measurement.

There was a previous attempt to use SHS in the LWIR by a group at the Los Alamos National Laboratory. Preliminary results from this effort were published;[14] however, the project was terminated before a broadband LWIR SHS spectrum was successfully recorded.

The primary goals of this work are: 1. to demonstrate that SHS can be used for high-resolution LWIR spectroscopy by measuring broadband spectra in the laboratory, and 2. to show that a field-widened LWIR SHS interferometer can be built in a rugged package using a mechanical structure fabricated with conventional machining tolerances and without the need for postintegration alignment. In the following sections we give a detailed description of the SHIMCAD instrument and laboratory measurements, provide some remarks on the instrumental background, and summarize the conclusions of this effort. The last section also provides a perspective on potential future work.

2 Instrument Description

The optical design of SHIMCAD consists of: 1. an anamorphic telescope that images one dimension of the scene onto the interferometer gratings, 2. an SHS interferometer that modulates this scene with interference fringes from which the spectrum is derived, and 3. exit optics that transfer the scene/fringe image onto the focal plane array. A sketch of the imaging scheme from the telescope field of view to the focal plane array (FPA) is shown in Fig. 1. A scale drawing of the entire optical train and a corresponding photograph showing each of the subassemblies is shown in Figs. 2(a) and 2(b).

2.1 *Telescope*

The anamorphic SHIMCAD telescope consists of both cylindrical and spherical, antireflection coated, germanium (Ge) refractive elements. The telescope images the scene in the vertical dimension onto the pupil of the SHS interferometer assembly. In the horizontal direction the telescope objective is imaged onto the diffraction gratings so that light from every spatial point in the scene (at infinity) illuminates the full width of the interferometer. Any spatial information of the scene in the horizontal dimension is thereby averaged over each horizontal slice on the grating, which ultimately eliminates the contamination of the spectral information that is contained in the intensity modulation superimposed by the interferometer in this dimension. Thus, in the final image on the FPA, the vertical dimension of the detector is used for spatial information and the horizontal dimension is used to recover the spectral information (see Fig. 1).

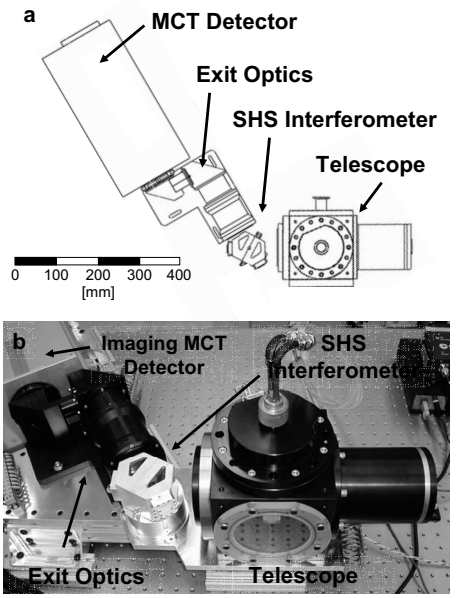

Fig. 2 (a) Scale drawing of the SHIMCAD optics comprising the telescope, field-widened interferometer, exit optics, and imaging detector. (b) Photograph of SHIMCAD optics. The entrance aperture is located on the right of the telescope.

The front aperture of the telescope is 61×20 mm and the SHIMCAD field of view is approximately 4×4.5 deg. The telescope is built into a vacuum chamber that has a cooled field stop that limits the speed of the beam onto the grating to f/6.3 in the horizontal (spectral) dimension, and to f/2 in the vertical (imaging) dimension. The speed of the beam onto the grating in the vertical (imaging) dimension was chosen to match the fastest beam the detector assembly could accept. In the horizontal (spectral) dimension the speed of the beam is limited to f/6.3 to avoid background signal from unwanted, higher grating orders.

Also located in the imaging telescope is a cooled, broadband interference filter with a spectral passband that matches the width of a single interferometer side band (see Table 1 in Sec. 2.2 for filter and instrument passband specifications). A thermoelectric cooler (TEC) in the telescope cools both the field stop and filter to $-10\ ^{\circ}\mathrm{C}$. Except for the mercury cadmium telluride (MCT) detector, none of the other SHIMCAD components are cooled.

2.2 *Interferometer*

A sketch of the optical components of the SHIMCAD interferometer and raytrace is shown in Fig. 3. The interferometer comprises a compensated ZnSe 50/50 beamsplitter (BS), antireflection coated Ge field-widening prisms (P1

Table 1 Spectrometer design specifications.

Parameter	Design value
Telescope	
Field of view	4 deg(h) × 4.5 deg(v)
Aperature size	61 mm(h) × 20 mm(v)
Filter temperature	−10 °C
Filter blue cut-on (T=20%)	1196 cm^{-1} (as built)
Filter red cut-off (T=20%)	862 cm^{-1} (as built)
Interferometer	
Beamsplitter	ZnSe (compensated)
Gratings	
Grating angle	7.24 deg
Grating groove density	30 mm^{-1}
Illuminated grating area	9.6 mm(h) × 7.2 mm(v)
Field of view at the gratings	28.07 deg(h) × 9.08 deg(v) [full angle]
Prisms	
Prisms size	20 mm(h) × 15 mm(v)
Prism thickness (at center)	5.0 mm ± 0.0 mm
Prism apex angle	1.9 deg
Prism angle of incident	4.1 deg
Maximum resolution (unapodized)	2 cm^{-1}
Maximum passband	870 to 1190 cm^{-1}
Etendue	4.7×10^{-5} m^2 sr
Littrow wavenumber	1190 cm^{-1}
MCT detector	
Size and pitch	320 × 240, 30 μm
FPA operating temperature	70 K

and P2), and reflective diffraction gratings (G1 and G2). The interferometer's beamsplitter is used with a 30-deg angle of incidence to minimize polarization effects and therefore maximize the signal-to-noise ratio of the measurement.

The ray trace was performed using Zemax (Zemax, Bellevue, Washington). The individual arms are treated as separate configurations and are subsequently superposed. All wavelengths enter the interferometer from the telescope (lower left of Fig. 3) with the same beam footprint. The increase in beam size at the exit of the interferometer is due to dispersion occurring at the diffraction gratings.

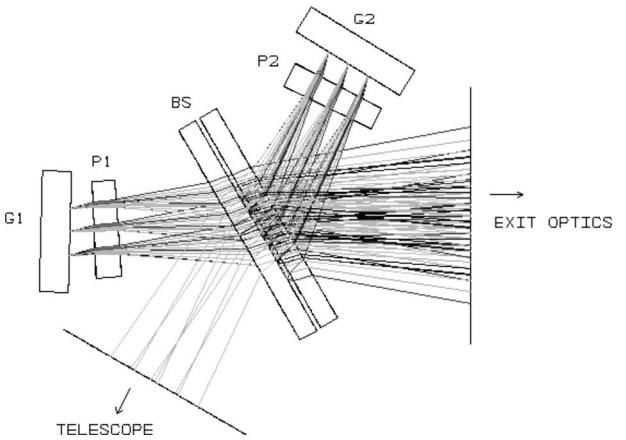

Fig. 3 Schematic of the SHIMCAD interferometer showing a ray bundle received from the input telescope and the output ray bundle feeding into the exit optics. The input beam consists of all wavelengths in the instrument passband and is dispersed by the gratings, resulting in a wider beam pattern at the interferometer exit. (BS: ZnSe compensated beamsplitter; P1/2: germanium field widening prism; G1/2: grating.)

The gratings of the interferometer are used in first order and tilted by 7.24 deg, the Littrow angle for $\lambda = 8.4$ μm ($\sigma = 1190$ cm^{-1}). Consequently, signal at the Littrow wavelength produces a fringe pattern with zero spatial frequency at the detector. A signal with $\lambda = 11.5$ μm ($\sigma = 870$ cm^{-1}) produces a fringe pattern with 160 fringes across the width of the detector. This corresponds to the Nyquist limit of observable fringes, as the detector has 320 pixels in the spectral (horizontal) dimension. Table 1 summarizes some important design parameters of the SHIMCAD spectrometer.

The interferometer's primary mechanical structure is machined out of aluminum. Critical dimensions were fabricated with a tolerance requirement of 13 μm ($\approx 1/2000$ in.), which is achievable with current state of the art computer numerical controlled (CNC) machines. The structure is constructed in two halves that sandwich the beamsplitter and compensator plate. The prisms are registered to this beamsplitter assembly, and a wedged hollow aluminum spacer in each arm between the prism and grating provides the alignment between them. The prism, spacer, and grating assembly is held in compression with a spring-loaded plunger system that keeps the elements registered to three position pads in each interferometer arm. This mechanical design proved to be effective in accurately aligning both arms of the interferometer to within machine tolerances, so that no external adjustments were required. When assembled, the aluminum structure and optical elements form a rugged, compact, field-widened interferometer.

For an SHS interferometer, the spectral resolution, or the distance between two independent spectral samples $\delta\sigma$, is the inverse of twice the maximum optical path difference measured in the interferogram, similar to a conventional Fourier transform spectrometer.[9,15] When an apodizing function is applied to the interferogram, to minimize side lobes of the instrumental line shape function, the resolution is reduced depending on which function is used.[16,17]

Typically, the resolution of SHS instruments is specified using the resolving power, which is the ratio of $\delta\sigma$ and the observed wavenumber ($R=\delta\sigma/\sigma$).[9] This is most appropriate for instruments with narrow passbands where the relative change of σ is small within the passband. SHIMCAD, however, covers a comparatively wide passband, so it is more appropriate to specify its resolution using the constant distance between independent spectral samples or the full width at half maximum of the instrumental line shape function. (Strictly speaking, the sample width in an SHS instrument is not constant due to the nonlinearity of the grating equation, but even for this relatively broadband instrument, this effect is very small.)

For most SHS instruments, including SHIMCAD, the spectral resolution is dominated by the grating dispersion, with the field widening prisms making only a small contribution. Without interferogram apodization, SHIMCAD was designed to a have a resolution of 2 cm^{-1}. As discussed in Sec. 3, we applied a Hamming apodizing function to the measured data, which suppresses the side lobes of the instrumental line shape function and decreases the resolution by a factor of about 1.8.[16,17] Thus, SHIMCAD is expected to achieve a resolution of about 4 cm^{-1}.

It is important to note that without field widening the beam divergence at the gratings for this resolution would be limited to a full angle of 6.73 deg (f/8.5) in both dimensions. The resulting etendue gain for SHIMCAD when compared to a nonfield-widened interferometer is approximately 5.7.

2.3 *Exit Optics and Detector*

The SHIMCAD exit optics reimage the scene from the gratings onto the detector with unit magnification, and correct for astigmatism introduced by the compensated plate beamsplitter in the interferometer. The detector is a mercury cadmium telluride (MCT) focal plane array manufactured by Cedip, model Jade VLWIR, with 320 $\times$240 pixels and a pixel pitch of 30 μm. The focal plane array is cooled to 70 K using an internal sterling cooler. The Jade camera has a cold vacuum shroud surrounding the FPA, which limits the maximum speed of the incoming beam to a full angle of 28.07 deg (f/2).

3 Laboratory Measurements

Transmittance measurements of two sample types were acquired with SHIMCAD, providing the first broadband LWIR spectra measured by a spatial heterodyne spectroscopy instrument. First, the transmittance of a direct path absorption cell, filled with different amounts of methanol gas, was measured. Second, transmittance features of a thin film of polyimide (Kapton®, Dupont Electronics, Wilmington, Delaware) were measured. Both sample types have distinct absorption features within the SHIMCAD passband, which allow the determination and verification of the Littrow wavenumber and the spectral sampling of the as-built interferometer.

In the following section we discuss the measurement approach, which is identical for both sample types, and the individual results.

3.1 *Measurement Approach*

For all measurements discussed here, the SHIMCAD entrance aperture was reduced by about 35% to 40$\times$20 mm to match the clear aperture of the direct path absorption cell used for the methanol sample. This reduction was accomplished by a single room temperature iris directly in front of the telescope. Thus, the blocked part of the telescope presented a constant, room temperature background contribution.

The samples were placed between the telescope aperture and a 100 °C blackbody source (CI systems, model CI-SR80, 9$\times$9 cm, CI Systems, Simi Valley, California). All transmittances T were determined using "source-off" corrected measurements:

$$T=\frac{B_S^{\mathrm{on}}-B_S^{\mathrm{off}}}{B_0^{\mathrm{on}}-B_0^{\mathrm{off}}}, \tag{1}$$

where B_S^{on} and B_0^{on} are measurements with the instrument viewing the blackbody source through the sample (filled cell or Kapton®) and without the sample (empty cell or no Kapton®), respectively. B_S^{off} and B_0^{off} are "source-off" measurements with and without the sample and the blackbody source blocked by a virtually nonemitting cold surface. We used a sheet of Eccosorb® (Emerson and Cumings Microwave Products, Randolf, Massachusetts), a porous microwave absorber, soaked in liquid nitrogen (77 K) for this cold surface. Since the spectral radiance of a 77 K blackbody radiation around 1000 cm^{-1} is more than a million times lower than that at room temperature, we assume that this cold surface does not emit within the SHIMCAD passband. The source-off correction can be performed in the interferogram or the spectral domain. We chose to perform it in the interferogram domain.

Using the approach of Eq. (1) eliminates any contributions from the emission of the sample itself and contributions from portions of the field of view that do not view through the sample, both of which would contaminate the result.

Individual measurements were taken with an integration time of 400 μs, and averages of 400 exposures were formed to increase the signal-to-noise ratio. Thus, the total integration time of each measurement was 160 ms, and the total measurement time for each average was about 7 s.

The measurements were also flat-field corrected, using the "unbalanced arm" flat fielding approach described by Englert and Harlander.[18] This approach requires two additional measurements, each with one of the interferometer arms blocked. To accomplish these measurements, we again used an Eccosorb® strip, soaked in liquid nitrogen, and inserted it between the beamsplitter and the field-widening prisms.

Corrected interferograms were transformed into power spectra, removing any phase information. Thus, the interferograms were not phase corrected prior to the transformation. Phase correction can generally be performed on SHIMCAD data and is expected to further increase the signal-to-noise ratio of the spectra.[19]

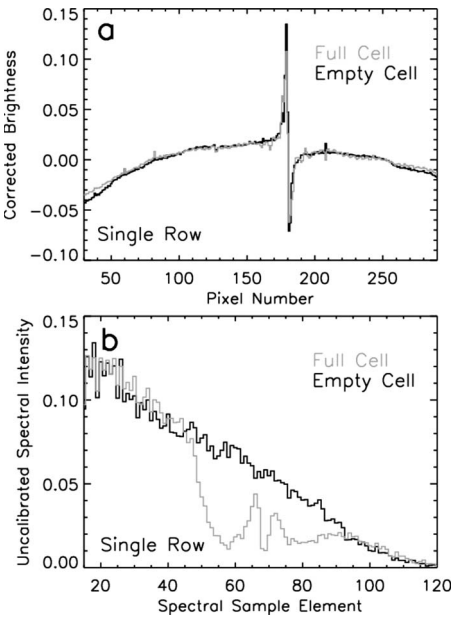

Fig. 4 (a) Source-off and flat field corrected single row interferograms for an empty cell and a methanol pressure of 26.9 hPa. (b) Power spectra of the interferograms shown in (a). The unresolved band structure of the methanol absorption is clearly visible in the "full cell" spectrum.

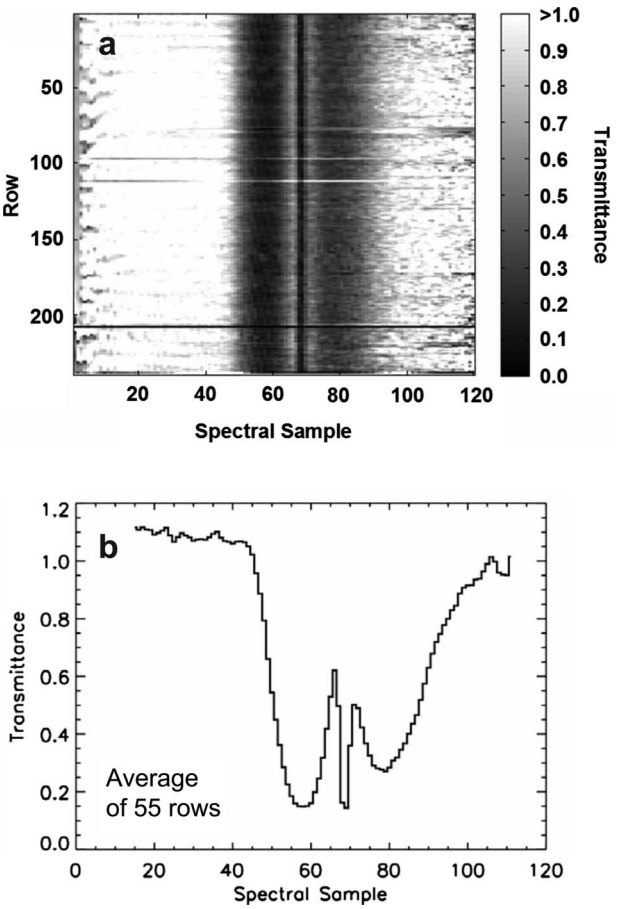

Fig. 5 (a) Methanol transmittance spectra calculated for the dataset shown in Fig. 4. All 240 rows are displayed. (b) Average of 55 rows.

3.2 *Methanol*

Methanol was chosen as a sample gas, since it has a strong ro-vibrational band within the SHIMCAD passband. The absorption features of this band originate mainly from the fundamental CO stretch mode. Furthermore, methanol is easy to handle in the laboratory. The measurements were performed using a 50-mm-long, direct path absorption cell with a clear aperture of 41 mm. The cell windows were made of broadband antireflection coated germanium, and it was equipped with pressure and temperature sensors.

Examples of source-off and flat field corrected interferograms are shown in Fig. 4(a) for an empty cell and a methanol pressure of 26.9 hPa (full cell). Note that the interferograms shown here represent data gathered from only a single row of the focal plane array. The zero path location is easily identified as the interferogram spike around pixel number 180, close to the middle of the 320-pixel-wide FPA. The shape of the spike is an indication of a phase issue due to a slight misalignment of the gratings, which is commonly seen in the phase of SHS interferograms and, in general, does not have any negative impact on the measurements. Effects related to the fringe phase due to minor misalignments, optical defects, or index inhomogeneities can, in fact, be easily corrected during the data analysis.[10,19] As mentioned before, only the power spectra are calculated from the interferograms, thus phase shifts do not propagate into the spectra.

As shown in Fig. 4(a) away from the zero path location, the corrected interferograms are not flat, as expected for a broadband source. This is likely due to the fact that the flat field measurements are not perfect, and possibly also due to instrument drifts between the measurements. Assuming that this effect is multiplicative in the interferogram domain, it will result in a slight change of the instrumental line shape function in the spectral domain.

Lastly, we point out that we used a Hamming function to apodize the interferograrm, and we truncated the interferogram at the highest optical path differences because the illumination at these locations was poor. This results in a slight reduction of resolution.

Figure 4(b) shows the power spectra of the interferograms in Fig. 4(a). The methanol absorption band is clearly visible. Also noteworthy is the decline in signal for increasing spectral sample number, which is equivalent to decreasing fringe modulation for increasing fringe frequency in the interferogram. The steep decline could be due to the fact that the exit optics are not optimally focused or an internal alignment problem of the exit optics, which degrades its modulation transfer function.

Since SHIMCAD uses a 2-D detector array, each exposure allows the calculation of a transmittance spectrum for each row of the FPA. Figure 5(a) shows a grayscale image of all 240 transmittance spectra. Since the setup we used did not contain any spatial information in the vertical dimension, which is imaged on the FPA, the spectra are virtually identical for each row. The small number of rows that appear to contain different spectral information are contaminated by single, defective pixels that are not properly

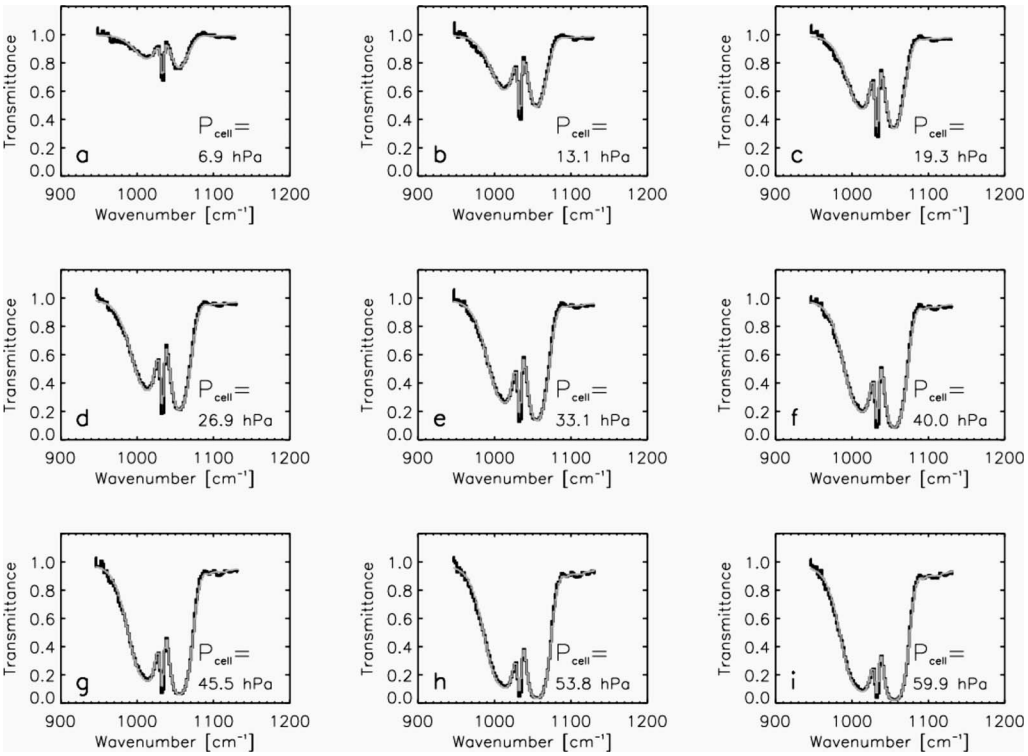

Fig. 6 (a) through (i) Baseline corrected methanol transmittance spectra measured by SHIMCAD are shown in black. The gray lines are best fit theoretical transmittance curves. The Littrow wavelength, sample spacing, baseline offset and slope, and cell pressure were used as parameters in the fit algorithm. Cross sections were taken from NIST.[20]

corrected during the flat fielding process. These effects can easily be eliminated with a more sophisticated flat fielding algorithm.

Figure 5(b) shows an average of 55 rows that are not affected by the previously mentioned flat fielding issues. Again, the methanol absorption band structure is clearly visible. It is also apparent that there is a slight baseline drift over the period of time the measurements for this transmittance spectrum were taken, since the transmittance values exceed unity.

Methanol transmittance measurements were conducted for a total of nine different pressures. Due to the unreliability of the pressure sensor at low pressures and the increasing opacity of the sample for higher pressures, the cell pressures for these measurements range from 6.9 to 59.9 hPa. Figure 6 shows the results for all nine measurements. For this figure, the measurements were baseline corrected using a best fit, multiplicative, linear baseline to account for the slight instrument drift.

Also shown in Fig. 6 are best fit theoretical transmittance spectra. To find the best fitting spectra, we used a nonlinear least squares fit algorithm with the following parameters: baseline offset, baseline slope, Littrow wavenumber, sample spacing, and the pressure in the cell. Methanol absorption cross sections with a resolution of 0.125 cm^{-1}, published by the National Institute of Standards, were used in the fit algorithm.[20] We determined the Littrow wavenumber to be 1172.35 ($\pm$1.34) cm^{-1} and the sample spacing to be 2.06 ($\pm$0.02) cm^{-1}, both of which are sufficiently close to the design values (see Table 1). It is worth noting that the Littrow wavenumber is just slightly on the long wavelength side of the short wavelength cut-off of the filter. This results in a contamination of about the first 20 spectral samples, since for those, signal from both sides of the Littrow wavenumber is superposed. However, the first several samples of a conventional, single side band SHS spectrum are often not used anyway, due to the typically low filter transmittance and the potential contamination by low frequency noise.

For the fit of the data shown in Fig. 6, the instrumental line shape function was assumed to be Gaussian in shape, with a full width at half maximum of 4 cm^{-1}, allowing for the decrease in spectral resolution due to the interferogram apodization with a Hamming function. Unfortunately, the broad features of the unresolved methanol absorption spectrum do not allow us to determine the exact value of the instrumental line width by including it as a parameter into the fitting algorithm.

Figure 7 shows the cell pressures retrieved from the transmittance measurements versus the pressures measured by the pressure sensor of the absorption cell. Even though the pressures show a very good linear correlation, a linear fit to the data shows a nonzero offset and a slope that is significantly different from unity. This result is likely due to a combination of the following effects. First, the measurements are not optically thin; the cross sections used for the fit were measured at one atmosphere and the absorption lines in the cross section measurement are not fully resolved at 0.125 cm^{-1}. Second, a nonzero offset of the pressure sensor at small pressures cannot be ruled out. Third,

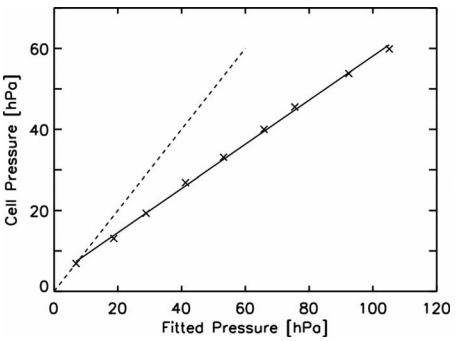

Fig. 7 Methanol pressure determined from the cell pressure sensor versus the methanol pressure determined by the nonlinear least squares fit to the transmittance spectra shown in Fig. 6. The solid line is a fit through the measured points. The dashed line indicates a perfect correlation.

multiple passes through the cell, caused by partial reflection on the cell windows, which are effectively increasing the cell length, cannot be ruled out.

Clearly, our simple setup and analysis approach does not warrant any high accuracy quantitative analysis of this methanol absorption data. That would require much more care in cell design, pressure, and temperature instrumentation, optically thin measurements, and more suitable cross section data. However, these data are surely well suited to demonstrate the feasibility of spatial heterodyne spectroscopy for the LWIR, which was the main goal of this work.

3.3 *Kapton® Spectrum*

The second sample type measured for this work was a 25-μm-thick polyimide (Kapton®) foil. Measuring the external transmittance of a foil eliminates any issues with absorption cell windows; however, reflections on both surfaces of the foil and ensuing multiple beam paths within the foil cause the well known effect of channel spectra that present a significant contribution to the external transmittance. Moreover, this effect depends on the incident angle of the transmitting beam and the distribution of intensity versus angle within the beam. Recognizing these nontrivial effects, we are seeking a qualitative comparison of a SHIMCAD measurement to an independent measurement. For this purpose, we use a measurement performed by a Fourier transform spectrometer.

Figure 8 shows the FTS and SHIMCAD measurements for comparison. The main features of the polyimide absorption shown in the FTS measurement are clearly well reproduced by the SHIMCAD measurement. Again, due to the different beam geometry, the measurements are not expected to yield identical transmittance spectra.

The spectral scale of the SHIMCAD measurement shown in Fig. 8(b) is calculated using the Littrow wavenumber and sample spacing determined from the methanol measurements.

4 Instrumental Background

For LWIR spectrometers that comprise a room temperature structure and optics, special care has to be taken in the design to avoid large instrumental background signals that generally decrease the signal-to-noise ratio of the measurement. As discussed in Sec. 2, the goal in the SHIMCAD optical design was to minimize the background signal by cooling only the interference filter and field stop. Furthermore, we tried to optimize the imaging optics between the interferometer and the detector, so that the f/2 beam accepted by the camera assembly comprises only parts that pass through the telescope and parts that view either the cooled field stop or are reflected back into the cooled detector dewar. This way the signal from the room temperature interferometer structure should be minimized.

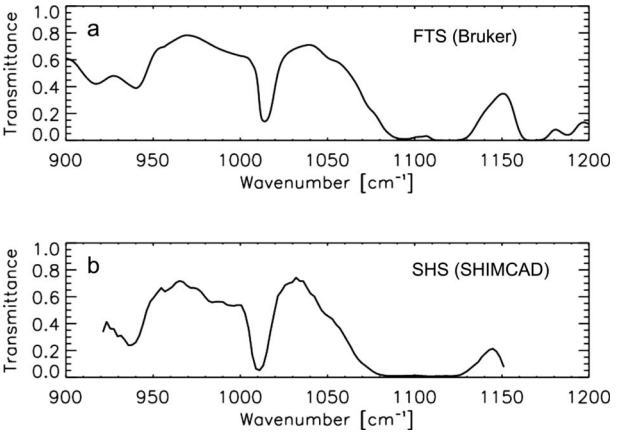

Fig. 8 (a) Polyimide (Kapton®) 25-μm-thick film external transmittance measured with a FTS (Bruker) at 1-cm^{-1} resolution. (b) External transmittance of the same sample measured by SHIMCAD. Qualitatively the measurements match very well. Since the beam geometry and sample orientation are slightly different for both measurements, they are not expected to be identical.

To assess the instrumental background signal, we made measurements of a cold blackbody source (Eccosorb® soaked with liquid nitrogen) at several positions in the optical train. Using the mean signal readout from the detector array as a measure of the signal incident on the focal plane array, we found the following relative background and signal contributions: the camera assembly contributes 28%, the exit optics contribute 34%, the interferometer 8%, the telescope 3%, and a room temperature scene contributes 26% to the total signal incident on the detector.

Two major conclusions can be drawn from this result. First, the contribution from in-band and out-of-band light that is emitted by the interferometer gratings or originates at the room temperature surfaces of the spectrometer structure and is scattered and diffracted onto the field of view of the detector pixels by the interferometer is consistent with high efficiency gratings, and thus does not dominate the total signal. Second, the performance of the exit optics is not as high as expected. The reason for its high background contribution (34%) needs to be investigated and is anticipated to lead to an improved exit optics design. This effort, however, is out of the scope of this work.

Assuming pure shot noise, a constant signal from the observed scene, and a constant integration time, the noise equivalent spectral radiance (NESR) of the measurement is proportional to the square root of the inverse of the total signal detected at the imaging array. Therefore, if for example, the exit optics contribution can be reduced from 34 to 5%, the NESR would be reduced by about 16%. The

elimination of all instrumental background sources would result in an NESR reduction of about 50%. These estimates are based purely on shot noise and do not include read noise or systematic uncertainties introduced by the radiometric calibration, instrument drifts, flat fielding, or phase distortion corrections.

5 Conclusions

We present the design and implementation of an LWIR SHS interferometer. We also show and discuss the first successful, broadband, SHS LWIR measurements, which establish SHS within the field of LWIR spectroscopy.

The SHS interferometer used here exhibits a rugged monolithic design, in which all components are self aligned and held in compression. The interferometer is designed without any option of postintegration alignment, and it is shown successfully that conventional machine tolerances are sufficient to assure proper alignment of the optical components.

The transmittance of two sample types, a direct path absorption cell filled with methanol and a polyimid foil sample, are measured and the data analysis is discussed. For both sample types, the measurement results successfully demonstrate the feasibility of using SHS in the LWIR. Systematic sample properties like potential multipath beams in the absorption cell and foil sample, opacity issues, and available cross section resolution prevented a more quantitative verification of the measurements; however, this was not the goal of this work and is ultimately out of the scope for this project.

Two specific spectrometer issues were identified that can and should be addressed in future work: 1. higher than expected instrumental background, and 2. sensitivity decrease for high spatial frequencies, possibly due to the exit optics modulation transfer function or focus.

In addition to these remaining instrument issues, future work should include field measurements, the detailed investigation of instrument stability, and the required frequency of calibration measurements. Ultimately, a field hardened SHS LWIR instrument is envisioned, taking advantage of the specific SHS properties that make it attractive for applications in rugged environments and on moving platforms. Namely, the inherent ruggedness, lack of moving parts, and insensitivity to a changing scene, avoiding the need for stabilized pointing and staring platforms.

Acknowledgments

We acknowledge the Office of Naval Research for funding this work. We thank Ronen Feldman, Charles M. Brown, W. Layne Marlin, Jeffrey H. Bowles, Daniel R. Korwan, CDR J. Tim Bays (USNR), and Andrew N. Straatveit for their support. We also thank Kenneth P. Stewart and Jacqueline Fischer for providing the FTS measurements of polyimide.

References

1. P. G. Lucey, T. J. Williams, M. Mignard, J. Julian, D. Kobubun, G. Allen, D. Hampton, W. Schaff, M. J. Schlangen, E. M. Winter, W. B. Kendall, A. D. Stocker, K. A. Horton, and A. P. Bowman, "AHI: an airborne long wave infrared hyperspectral imager," *Proc. SPIE* **3431**, 36–43 (1998).
2. J. P. Allard, M. Chamberland, V. Farley, F. Marcotte, M. Rolland, A. Valliéres, and A. Villemaire, "Airborne measurements in the long-wave infrared using an imaging hyperspectral sensor," *Proc. SPIE* **7086**, 70860K (2008).
3. E. R. Schildkraut, R. F. Connors, A. Ben-David, and A. I. Ifarraguerri, "An ultra-high sensitivity passive FTIR sensor (HiSPEC) and initial field results," *Proc. SPIE* **4574**, 18–25 (2002).
4. B. Hammond and M. Popa, "Overview of the joint services lightweight standoff chemical agent detector (JSLSCAD)," *Proc. SPIE* **5795**, 86–95 (2005).
5. R. Harig, J. Gerhard, R. Braun, C. Dyer, B. Truscott, and R. Moseley, "Remote detection of gases and liquids by imaging Fourier transform spectrometry using a focal plane array detector: first results," *Proc. SPIE* **6378**, 637816 (2006).
6. W. Wadsworth and J. P. Dybwad, "Rugged high speed rotary imaging Fourier transform spectrometer for industrial use," *Proc. SPIE* **4577**, 83–88 (2002).
7. W. J. Marinelli, et al., "Tunable Fabry-Perot etalon-based long-wavelength infrared imaging spectroradiometer," *Appl. Opt.* **38**, 2594–2604 (1999).
8. J. A. Hackwell, D. W. Warren, R. P. Bongiovi, S. J. Hansel, T. L. Hayhurst, D. J. Mabry, M. G. Sivjee, and J. W. Skinner, "LWIR/MWIR imaging hyperspectral sensor for airborne and ground-based remote sensing," *Proc. SPIE* **2819**, (1996).
9. J. M. Harlander, R. J. Reynolds, and F. L. Roesler, "Spatial heterodyne spectroscopy for the exploration of diffuse interstellar emission lines at far ultraviolet wavelengths," *Astrophys. J.* **396**, 730–740 (1992).
10. J. M. Harlander, H. T. Tran, F. L. Roesler, K. P. Jaehnig, S. M. Seo, W. T. Sanders, and R. J. Reynolds, "Field-widened spatial heterodyne spectroscopy: correcting for optical defects and new vacuum ultraviolet performance tests," *Proc. SPIE* **2280**, 310–319 (1994).
11. C. R. Englert, M. H. Stevens, D. E. Siskind, J. M. Harlander, F. L. Roesler, H. M. Pickett, C. von Savigny, and A. J. Kochenash, "First Results from the spatial heterodyne imager for mesospheric radicals (SHIMMER): diurnal variation of mesospheric hydroxyl," *Geophys. Res. Lett.* **35**, L19813, doi: (2008).
12. O. R. Dawson and W. M. Harris, "Tunable, all-reflective spatial heterodyne spectrometer for broadband spectral line studies in the visible and near-ultraviolet," *Appl. Opt.* **48**, 4227–4238 (2009).
13. J. E. Lawlor, Z. E. Labby, J. M. Harlander, and F. L. Roesler, "Broadband, high-resolution spatial heterodyne spectrometer," *Appl. Opt.* **47**, 6371–6384 (2008).
14. B. E. Laubscher, B. W. Smith, B. J. Cooke, P. C. LaDelfe, R. R. Berggren, P. V. Villeneuve, R. M. Goeller, G. M. Obbink, S. Milligan, J. W. Howard, P. R. Norton, M. Stegall et al., "The infrared imaging spatial heterodyne spectrometer (IRISHS) experiment effort," *Proc. SPIE* **3701**, 194–205 (1999).
15. J. W. Brault, "Fourier transform spectroscopy," in *High Resolution in Astronomy: Fifteenth Advanced Course of the Swiss Society of Astronomy and Astrophysics*, A. Benz, M. Huber, and M. Mayor, Eds., Geneva Observatory, Sauverny, Switzerland, pp. 1–61 (1985).
16. R. H. Norton and R. Beer, "New apodizing functions for Fourier spectrometry," *J. Opt. Soc. Am.* **66**, 259–264 (1976).
17. D. A. Naylor and M. K. Tahic, "Apodizing functions for Fourier transform spectroscopy," *J. Opt. Soc. Am.* **24**, 3644–3648 (2007).
18. C. R. Englert and J. M. Harlander, "Flatfielding in spatial heterodyne spectroscopy," *Appl. Opt.* **45**, 4583–4590 (2006).
19. C. R. Englert, J. M. Harlander, J. G. Cardon, and F. L. Roesler, "Correction of phase distortion in spatial heterodyne spectroscopy," *Appl. Opt.* **43**, 6680–6687 (2004).
20. *NIST Chemistry WebBook*, P. J. Linstrom and W. G. Mallard, Eds., NIST Standard Reference Database Number 69, National Institute of Standards and Technology, Gaithersburg MD, 20899, see http://webbook.nist.gov (retrieved 12 Mar 2009).

Christoph R. Englert received his DiplPhys degree in physics from the Technical University of Munich (Germany) in 1996, and a Dr rer nat in physics from the University of Bremen (Germany) in 1999. The research for his doctorate degree was performed at the German Aerospace Center (DLR). From 1999 to 2001 he held a National Research Council postdoctoral associateship at the Space Science Division of the Naval Research Laboratory (NRL). In 2001 he joined the staff at NRL, where he is currently the head of the planetary atmospheres section. His research interests include optical remote sensing, satellite instrumentation, the investigation of the Earth's upper atmosphere and planetary atmospheres.

David D. Babcock received his PhD in Earth and space science from Toronto's York University in 2006, and a BSc in physics from Mount Allison University in 1997. Working currently as a contract research physicist at the U.S. Naval Research Laboratory's Space Science Division in Washington D.C., his research interests involve optical spectroscopic and Doppler interferometry as applied to upper atmospheric research.

John M. Harlander received his MS in physics from the University of Wisconsin-Madison in 1986 and a PhD in physics from the University Wisconsin-Madison in 1990. In 1991 he joined the Department of Physics, Astronomy and Engineering Science at Saint Cloud State University, Minnesota, where he currently is a professor. He is past president of the Minnesota chapter of the Optical Society of America. His research interests include the development of interference spectrometers with applications in optical remote sensing, satellite instrumentation, the investigation of the Earth's upper atmosphere and astrophysics.